On the Aerodynamics of an Electric Vertical Take-off and Landing Aircraft Using Lattice Boltzmann Method

Reng Mo (莫礽),[1] Quan Zhou (周铨),[1] Qing Jia (贾青),[1] Chao Xia (夏超),[1] Huanxia Wei (韦欢夏)*,[2,1] and Zhigang Yang (杨志刚)[1,3]

[1)]*School of Automotive Studies, Tongji University, Shanghai, 201804, China*

[2)]*Department of Mechanical and Aerospace Engineering, University of Manchester, Manchester, M13 9PL, UK*

[3)]*Beijing Aeronautical Science and Technology Research Institute, Beijing, 102211, China*

(*Electronic mail: huanxia.wei@postgrad.manchester.ac.uk)

(Dated: 12 February 2026)

This study investigates the static stability and flow field of a cruising Electric Vertical Take-off and Landing (eVTOL) aircraft with compound-wing configuration using Lattice Boltzmann Method (LBM). Numerical accuracy of Finite Volume Method (FVM) and LBM is validated and comparatively analysed based on isolated rotor simulations. The LBM-based simulations are 8∼9 times faster than those based on FVM for weakly compressible flows, which exhibits significant advantages in computational efficiency and cost. The maximum error of thrust is ∼11% for LBM-based simulations, and that of torque is ∼7%, which is similar to that of FVM. Unsteady simulations based on LBM are conducted for the whole eVTOL aircraft, and flow field structures and static stability are further analysed. The results reveal that four varieties of vortical structures dominate the flow field, including wingtip and root vortices, vortices generated by static lift rotors, and vortices originating from the counter-rotating tail propeller pair, varying with angle of attack and angle of sideslip. Developing mechanisms and mutual interactions are examined in detail. The aircraft is unstable in terms of longitudinal and directional static stabilities, while it is stable in lateral enhanced by wingtip vortices. Besides, tail-mounted propulsion places higher demands on thrust propellers. Moreover, vortex generating at leading upper lift rotor edges delays separation on the wing upper surface, but imposes negative effects on both longitudinal and lateral stability. The high computational efficiency, accurate flow and realizable aerodynamic forces demonstrated by LBM provide engineering insights for future aerodynamic performance analysis and development of eVTOL aircraft.

Keywords. eVTOL aircraft, Lattice Boltzmann Method, Computational fluid dynamics, Static stability, Vortical structures

I. INTRODUCTION

The Electric Vertical Take-off and Landing (eVTOL) aircraft plays an important role in the future three-dimensional urban transportation system[1]. Compared to traditional helicopters, most types of eVTOL aircraft adopt compound-wing (also known as lift + cruise configuration) or multi-rotor designs, and have lower ceiling and airspeed, resulting in different aerodynamic performance.

Among all aerodynamic performance parameters, flight stability is the most critical aspect and receives much attention, as it is directly related to aviation safety. In conventional studies, mathematical models are developed and employed to predict the flight stability of aircraft. Based on the blade element theory, Pitt-Peters dynamic inflow theory and blade flapping motion model, He et al.[2] studied the flight stability of a compound-wing high-speed helicopter by establishing a comprehensive flight dynamics model. Wang[3] investigated the flight characteristics of an inter-meshing rotor helicopter by constructing a mathematical model in a similar way and evaluated its control capability. Luan[4] built a flight dynamics model of a compound-wing helicopter with two propellers, studied its stability, and then analysed the control performance by calculating dynamic and frequency responses. Wang et al.[5] established a non-linear flight dynamics model for a tilt-rotor aircraft, and

examined how variations in nacelle tilt angle affect eigenvalues and eigenvectors of motion modes as well as its stability derivatives. With the advancement of computational technique, it is also a common way to gain insights into flight stability through Computational Fluid Dynamics (CFD) simulations, and the modelling and simulation in the early stage of development can contribute to a better design process[6]. Various methods can be used in CFD simulations to capture the aerodynamic characteristics of propellers or rotors as well as the aircraft driven by them. Seaver et al.[7] compared the results of a flight test on lateral-directional stability with CFD simulations. The simulations were based on the Finite Volume Method (FVM), while zero-thickness disks with a specific pressure jump were used to simplify and substitute the actual physics of propellers. Kim et al.[8] found it efficient to apply actuator methods when simulating the propellers and analysing the longitudinal and directional flight stability of two distributed propulsion aircraft. Kim et al.[9] conducted Lattice Boltzmann Method (LBM) to quantify rotor-airframe aerodynamic interaction in hover by varying the airframe geometry (cylinder, cone) and the rotor-airframe separation distance. The computations captured tip vortex breakdown, transition to a turbulent wake, and proximity-induced modifications of the underbody fountain flow driven by rotor downwash circulation. Apart from these mid-fidelity methods, researchers have also adopted high-fidelity methods such as the sliding mesh approach[10] to represent the full blade accurately in numerical simulations, while novel grid setups such as a Cartesian off-body grid[11] have proven effective in representing blade rotation and elastic blade deformation. Gao et al.[12] employed unsteady Reynolds-averaged Navier-Stokes (uRANS) to resolve the dynamic stall vortex and trailing edge vortex evolution on a single rotor airfoil, validating the aerodynamic predictions against experimental data and relating vortex-driven unsteady pressure loading to the stall process. Moreover, CFD simulations facilitate the analysis of flow structures around the aircraft. Roh et al.[13] investigated the wake interaction around the tail propellers of a helicopter, thereby revealing the key factors in its directional stability. Similar technique was also demonstrated for helicopters with leading-edge slatted tailplane[14] and biplane tailplane[15]. Qi et al.[16] used detached-eddy simulation (DES) with overset mesh to quantify how a hovering coaxial rotor aerodynamically interacts with the ground and a nearby cubical obstacle at multiple relative positions. Su et al.[17] performed Reynolds-averaged Navier-Stokes (RANS) simulations with overset mesh to resolve the unsteady aerodynamic interactions among the upper and lower rotors, the ship flight deck, and the hangar door during vertical descent and landing. Green et al.[18] measured the flow field around an isolated rotor in axial descent, and Chae et al.[19] expanded this scenario to a pair of twin rotors, revealing the flow structures and thrust characteristics.

Nevertheless, as eVTOL aircraft represent a relatively recent concept, research into their aerodynamics remains in its early stages, with limited studies addressing the flight stability. Lee et al.[20] conducted a hover performance analysis of an eVTOL aircraft using a rotorcraft comprehensive analysis code, and identified effective control methods to enhance performance. Stokkermans et al.[21] conducted wind tunnel experiments on two propellers in side-by-side and one-after-another arrangements to quantify how axial and lateral spacing alters aerodynamic interaction penalties in thrust, power, in-plane forces, and out of plane moments, supported by total pressure and planar PIV measurements of the slipstream. Simmons et al.[22] developed a high-fidelity integrated aero propulsive model for the LA-8 tandem tilt-wing distributed electric propulsion (DEP) eVTOL using wind tunnel data obtained with design of experiments (DoE) methods, targeting coupled propeller wing interaction effects and high incidence propeller aerodynamics across the flight envelope. Based on the Vortex Particle Method (VPM), Zanotti et al.[23] performed mid-fidelity simulations to investigate the flow interactions between front and rear propellers. The thrust loss effect of the rear propeller was observed as the overlap between tandem propellers increased. Gao et al.[24] introduced a reformulated VPM approach to examine the aerodynamic performance of side-by-side propellers across varying advance ratios and angles of sideslip, and provided insights into the surrounding flow fields of the eVTOL aircraft. Araghizadeh et al.[25] employed a mid-fidelity framework with a stochastic turbulence inflow generator to assess how atmospheric turbulence modifies the rotor wake and aerodynamic loading of tandem eVTOL aircraft in cruise. It is concluded that incoming turbulence progressively disrupts and degrades wake coherence, enhances load instability, and promotes blade-vortex interactions. Later, they simulated a full configuration XV-15 tilt-rotor eVTOL during transition flight using VPM to resolve unsteady aerodynamic loads and wake development over varying nacelle tilt angles[26]. Liu et al.[27] did similar investigation on tilt-wing eVTOLs but

with high-resolution quasi-steady simulations, to characterize aerodynamic interference and wake evolution of multirotor tilt-wing eVTOL configurations during configuration conversion, comparing a single tilt-wing and a tandem tilt-wing layout. Deng et al.[28] conducted wind tunnel tests to characterize tilt-rotor eVTOL aerodynamics under coupled variations of propeller slipstream, angle of attack (AoA), aileron deflection, and flap deflection, deriving forces, moments, and aerodynamic coefficients. Luan et al.[29] combined test bench measurements with computational fluid dynamics to quantify how rotor dihedral angle and AoA under horizontal inflow reshape propeller upwash and downwash, thrust sharing among adjacent rotors, and overall force and moment responses. Bucherelli et al.[30] applied a mid-fidelity numerical framework with a staged buildup from an isolated rotor to a full aircraft configuration, to quantify inter-rotor and airframe interaction effects on rotor performance in hover and cruise. The simulations indicated limited interaction penalties in hover, whereas cruise exhibited stronger interactions. Sun et al.[31] performed numerical simulations to map how true airspeed, rotational speed, and tip clearance govern ducted fan aerodynamic performance for large-scale electric propulsion, establishing robust parametric correlations for thrust variation. Another line of related research falls onto the development of eVTOL aircraft with unique layouts or among diverse configurations. Chang et al.[32] proposed a tandem-channel wing layout for eVTOL aircraft. The longitudinal stability was analysed through CFD simulations based on FVM and the multiple reference frame method. Kim et al.[33] evaluated a specific eVTOL configuration using vortex lattice method, a low-fidelity analysis tool, and calculated the static margin under various conditions. However, directional and lateral stability analyses were not yet conducted.

It can be seen that the existing literature offers limited investigations on the flight stability of eVTOL aircraft, despite the critical importance of flight stability, especially in the early stages of aircraft development. Moreover, the majority of numerical simulations to date have relied on FVM, while few studies to date have employed the LBM method in this context. With the rapid development of GPU technology in recent years, the multi-core architecture of GPUs has significantly improved the efficiency in parallel floating-point operations, providing a novel computational paradigm distinct from conventional CPU-based huge clusters. In this regard, LBM stands out for its algorithmic simplicity, computational accuracy, and suitability for data distribution of parallel computing, making it especially effective for CFD computations on GPUs[34]. Additionally, LBM inherently incorporates discrete time terms, granting it a natural capability for unsteady simulations, which is essential for high-fidelity CFD simulations of rotating mechanisms such as rotors and propellers. LBM framework utilizes a Cartesian grid integrated with the immersed boundary method (IBM), and the numerical algorithm itself is inherently suitable for unsteady simulations with rotating machinery. A critical advantage of this approach is the elimination of interpolation-induced errors at the interfaces of rotating sub-domains, which are inherent in FVM for rotor simulations using sliding or overset mesh. Consequently, LBM could represent a highly efficient and promising approach for CFD simulations in eVTOL research. Nonetheless, also due to numerical methods, particularly boundary treatments, the numerical accuracy of LBM have prompted discussion by peers. A systematic study and analysis are urgently needed to quantitatively assess the reliability of LBM in industrial applications involving rotating machinery such as eVTOL aircraft by comparing against experiments.

We employ the LBM as a high-fidelity framework to resolve the unsteady fluid-dynamic mechanisms underlying eVTOL static stability. Dynamic stability such as phugoid and plunging modes remains outside the current scope, and will be further investigated in our future work. The numerical approach is validated against experimental study on an eVTOL lift rotor. A comparative evaluation between LBM and conventional FVM is performed in terms of numerical accuracy, computational power consumption and fidelity of rotor flow field representations. Accordingly, we demonstrate the multifaceted advantages of the LBM for eVTOL aerodynamic engineering and research as a GPU-accelerated, high-efficiency, high-fidelity numerical method, particularly well suited to rotorcraft applications. Subsequently, unsteady CFD simulations of the complete eVTOL configuration are conducted using the same LBM approach to capture time-resolved surrounding flow and wake features, enabling systematic analysis of longitudinal, directional, and lateral stability. The static stability characteristics are quantified by examining the variation of pitch moment with AoA, yaw moment with angle of sideslip, and roll moment with angle of sideslip, respectively, which are directly linked to asymmetric wake loading and unsteady pressure and shear-stress distributions. The

contributions of individual components to the overall static stability of the eVTOL aircraft are evaluated. Furthermore, the surrounding flow field of the eVTOL aircraft is visualized and analysed via pressure and velocity fields, vortical structures, and wake topology, thereby providing a comprehensive flow-based understanding of the stability behaviour of this eVTOL configuration and its governing factors.

The remainder of this paper begins with the description of LBM in Section II A and the validation of this numerical method in Section II B, followed by eVTOL modelling and computational setup in Section II C. The time-averaged and instantaneous flow fields of the eVTOL aircraft are shown in Section III A. The static stability characteristics are presented and discussed in Section III B. Finally, the conclusion is outlined in Section IV.

II. NUMERICAL SIMULATION

In this section, the theoretical basis of LBM is briefly introduced. The geometry of eVTOL used in this study and the numerical configurations are presented. The numerical accuracy of both LBM and FVM methods are validated by comparing with experimental data of the eVTOL rotor.

A. Lattice Boltzmann Method (LBM)

LBM is derived from the Boltzmann transport equation

$$\frac{\partial f}{\partial t}+\boldsymbol{\xi}\cdot\nabla f+\boldsymbol{a}\cdot\frac{\partial f}{\partial \boldsymbol{\xi}}=\Omega(f), \tag{1}$$

where f is the particle velocity distribution function, $\boldsymbol{a}$ denotes the particle acceleration, $\Omega(f)$ is the collision operator, and then gives

$$\begin{aligned}\boldsymbol{\xi}\cdot\nabla f&=\left(\frac{\mathrm{d}x}{\mathrm{d}t}\boldsymbol{i}+\frac{\mathrm{d}y}{\mathrm{d}t}\boldsymbol{j}+\frac{\mathrm{d}z}{\mathrm{d}t}\boldsymbol{k}\right)\cdot\left(\frac{\partial f}{\partial x}\boldsymbol{i}+\frac{\partial f}{\partial y}\boldsymbol{j}+\frac{\partial f}{\partial z}\boldsymbol{k}\right)\\&=u\frac{\partial f}{\partial x}+v\frac{\partial f}{\partial y}+w\frac{\partial f}{\partial z},\end{aligned} \tag{2}$$

$$\begin{aligned}\boldsymbol{a}\cdot\frac{\partial f}{\partial \boldsymbol{\xi}}&=\left(\frac{\mathrm{d}u}{\mathrm{d}t}\boldsymbol{i}+\frac{\mathrm{d}v}{\mathrm{d}t}\boldsymbol{j}+\frac{\mathrm{d}w}{\mathrm{d}t}\boldsymbol{k}\right)\cdot\left(\frac{\partial f}{\partial u}\boldsymbol{i}+\frac{\partial f}{\partial v}\boldsymbol{j}+\frac{\partial f}{\partial w}\boldsymbol{k}\right)\\&=\frac{\mathrm{d}u}{\mathrm{d}t}\frac{\partial f}{\partial u}+\frac{\mathrm{d}v}{\mathrm{d}t}\frac{\partial f}{\partial v}+\frac{\mathrm{d}w}{\mathrm{d}t}\frac{\partial f}{\partial w},\end{aligned} \tag{3}$$

where $\boldsymbol{i}$, $\boldsymbol{j}$ and $\boldsymbol{k}$ are the unit vectors in x, y and z coordinate directions respectively, u, v and w are the velocity components of the particle in these directions. Eq. 2 represents the change in the distribution function in physical space due to velocity, while Eq. 3 represents the change in the distribution function in velocity space due to acceleration.

LBM further discretises the Boltzmann equation along characteristic directions using probability distribution functions, thus obtaining the Lattice Boltzmann Equation (LBE)

$$f_i(\boldsymbol{x}+\boldsymbol{e}_i\Delta t,t+\Delta t)-f_i(\boldsymbol{x},t)=\Omega_i(\boldsymbol{x},t), \tag{4}$$

where i represents the characteristic direction, for which three-dimensional twenty-seven (D3Q27) lattice structure is employed in this study, $\boldsymbol{x}$ represents the physical space, $\boldsymbol{e}_i$ is the discrete velocity vector, Δt is the discrete time step, t denotes the current time; $f_i(\boldsymbol{x},t)$ denotes the particle distribution function at position $\boldsymbol{x}$, time t and along the direction of discrete velocity vector $\boldsymbol{e}_i$, $\Omega_i(\boldsymbol{x},t)$ represents the effect of particle collisions on the distribution function at position $\boldsymbol{x}$, time t along $\boldsymbol{e}_i$. Since it examines not the state of individual particles, but rather the state of all particles (i.e. the particle collective) within a sufficiently small control volume centred at the endpoint of the position vector, LBM describes fluid flow at the mesoscopic scale[35]. Through specific techniques,

the Navier-Stokes equations can be recovered from LBE[36], thereby demonstrating the macroscopic similarity between LBE and the original Navier-Stokes equations.

The core steps in the LBM iterative process are collision and streaming, and the specific procedure includes the following steps.

The fluid density $\rho(\boldsymbol{x},0)$, the velocity vector $\boldsymbol{u}(\boldsymbol{x},0)$ and the particle distribution function $f_i(\boldsymbol{x},0)$ are firstly initialised, then the equilibrium particle distribution function $f_i^{\mathrm{eq}}(\boldsymbol{x},t)$ are calculated. Next, the collision operator $\Omega_i(\boldsymbol{x},t)$ is to be computed. The Bhatnagar – Gross – Krook (BGK) model[37] is commonly used to simplify the collision operator:

$$\Omega_i(\boldsymbol{x},t) = \frac{1}{\tau}\left[f_i^{\mathrm{eq}}(\boldsymbol{x},t) - f_i(\boldsymbol{x},t)\right]. \tag{5}$$

The computation of post-collision distribution function $f_i^*(\boldsymbol{x},t)$ is then given by

$$f_i^*(\boldsymbol{x},t) = f_i(\boldsymbol{x},t) + \Omega_i(\boldsymbol{x},t), \tag{6}$$

and particle streaming is performed based on

$$f_i(\boldsymbol{x}+\boldsymbol{e}_i\Delta t, t+\Delta t) = f_i^*(\boldsymbol{x},t). \tag{7}$$

Afterwards, specific boundary conditions are applied, followed by the calculation of macroscopic quantities at time $t+\Delta t$ which includes fluid density ρ and velocity $\boldsymbol{u}$:

$$\rho = \sum f_i \quad \text{and} \quad \boldsymbol{u} = \frac{1}{\rho}\sum \boldsymbol{e}_i f_i. \tag{8}$$

Finally, repeat the iterative process above until the convergence criteria are met. The complete iteration is expressed as Fig. 1.

The pressure is calculated explicitly in the iteration using ideal gas equation:

$$p = \rho R T \tag{9}$$

where R is the specific gas constant, and T is the reference temperature.

LBM offers advantages such as solving linear equations instead of partial differential equations (PDE), which facilitates explicit computation and enables highly parallelised processing on GPUs, even for real-time simulation[38]. Furthermore, compared to conventional FVM solvers, LBM demonstrates superior performance and resolution in simulating complex geometries involving flow separation, moving boundaries, and fluid-solid interaction[39]. However, LBM has inherent limitations. In its basic form without corrective measures, it is restricted to low Mach number range and is facing challenges in accurately simulating high-speed and compressible flow[40]. Additionally, fluid velocity can erroneously propagate through solid boundaries of thin structures caused by the use of coarse Cartesian grids, resulting in non-physics fluid leakage[41].

In this study, LBM simulations are performed using a novel LBM platform, Aerocae (AEROCAE Digital, version 2025), based on the corrected LBM approach and Large Eddy Simulation (LES).

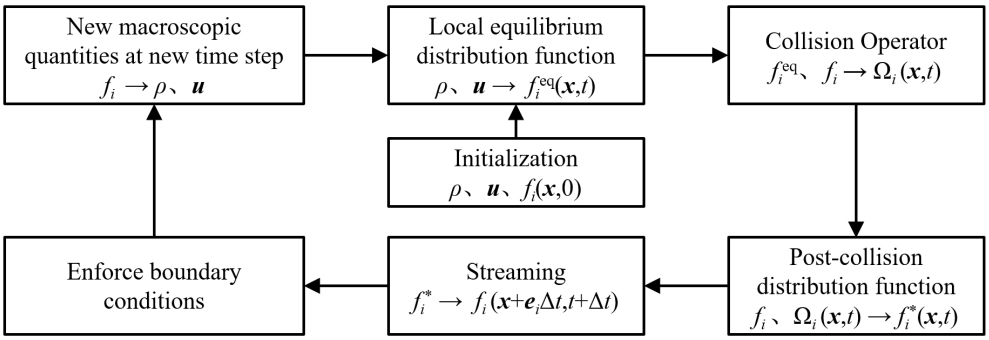

FIG. 1. LBM iterative flowchart.

The D3Q27 lattice structure is employed in the platform. While BGK collision model is a simplistic collision operator, there are significant truncation errors for simulations of high Reynolds number flows based on it since a single relaxation rate is used for all physical quantities. Therefore, a cumulant-based, multiple relaxation time collision model with an optimised higher-order relaxation rates developed by Lyu et al.[42] is adopted in the solver. To solve the turbulent boundary layer in an unsteady flow more accurately and efficiently and prevent numerical artifacts, a novel hybrid near-wall model by Liu et al.[43] is implemented, in which a macroscopic model and a mesoscopic model are combined, predicting a filtered wall velocity and reconstructing non-equilibrium distribution functions normal to the wall. For turbulence modelling, the Wall-Adapting Local Eddy-viscosity (WALE) sub-grid-scale (SGS) model[44] is used towards LES.

B. Validation

The eVTOL rotor in a hovering state is considered for validation of numerical results. Our eVTOL rotor, T-Motor $62'' \times 24''$, has two blades and a diameter of 62 inch (approx. 1.575 m) and made by carbon fibre. The geometry model (Fig. 2) is supplied by the manufacturer T-Motor as their precise model for manufacture. The experimental study is conducted using Series 1780 thrust & torque testing stand (Tyto Robotics, 2019) under varying rotational speed, and the operation of the rotor is powered by U15XXL Kv29 (T-Motor, 2019) and under the control of FLAME 280A HV (T-Motor, 2019) as the electronic speed controller of power system.

CFD simulations are conducted across a range of rotational speed from 1000 rpm to 2200 rpm based on both LBM-LES and FVM-LES numerical methods. As the comparative reference, the FVM-LES simulations are performed using Star-CCM+ (Siemens, version 2506). Low y^+ wall treatment with compressible implicit unsteady solver is selected. The computational domain is spatially discretized with hybrid polyhedral mesh to capture the tip vortices. The surface y^+ is ensured to be below 0.5 with the help of 20 prismatic layers under growth rate of 1.40. The final mesh cell count is 42.0 million. For the mesh strategy of LBM-LES, a six-level multi-resolution Cartesian grid is employed, with the minimum grid size of 3 mm and the outer size of 96 mm, as shown in Fig. 3.

During the validation stage, the FVM-LES simulation is conducted based on a workstation with a single Intel Xeon Platinum 8160T processor with 144 cores, while the LBM-LES simulation is performed on a consumer desktop PC with customised NVIDIA GeForce RTX 2080 Ti graphics card with 22 GB of GPU memory. The actual computational time of both numerical methods increases approximately linearly with the physical time in the simulations, showing no thermal

FIG. 2. CAD model of eVTOL rotor.

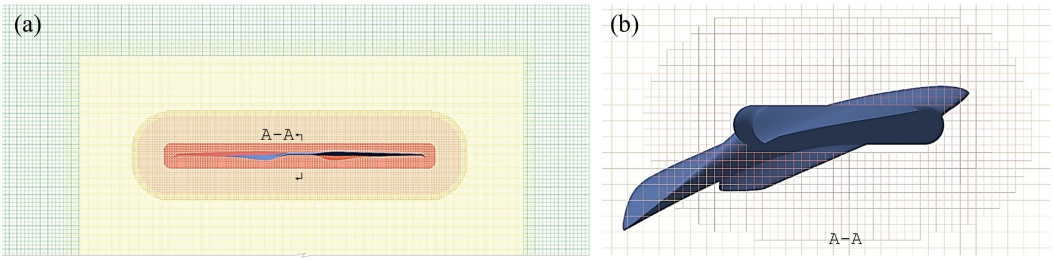

FIG. 3. Mesh sectional view of LBM-LES simulation on the eVTOL rotor. (a) mid-section, (b) a zoomed view.

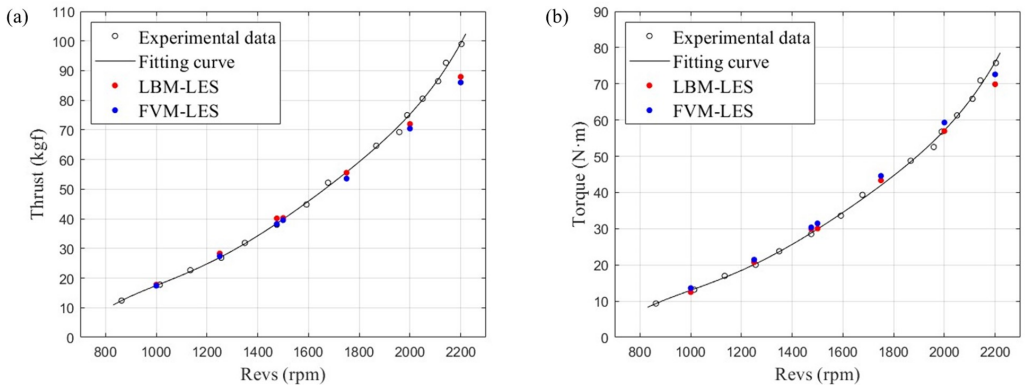

FIG. 4. Thrust and torque by the rotor versus rotational speed based on experimental results with fitting curve, LBM-LES and FVM-LES. (a) Thrust and (b) Torque.

performance degradation. For the same physical time, the LBM-LES simulation on the GPU is approximately 8∼9 times faster than FVM-LES on the CPU, substantially reducing the simulation time for each case and offering considerable effectiveness. Considering the variation in leasing costs of GPUs and CPUs, the financial advantage is more pronounced than the time savings.

The thrust and torque of the motor from both numerical and experimental studies are plotted in Fig. 4. It can be shown that the maximum error of the FVM-LES simulation is approximately 13% for thrust, while that of the LBM-LES simulation is about 11%. For torque, the maximum errors of both numerical methods are around 7%. It is also worth noting that, the thrust obtained by both methods begin to deviate evidently from the experimental values when the rotor speed reaches 2000 rpm. For torque data, the errors from both methods are smaller until the rotor speed reaches the highest 2200 rpm, although they still underestimate the torque. Overall, for both numerical methods, the errors in thrust and torque increase with rotor speeds, and their accuracy is comparable with each other. When the rotor speed reaches 2000 rpm, the tip Mach number is approximately 0.46, at which point the relative airflow near the rotor tip reaches a weakly compressible state. Given that the error margin is acceptable for most engineering applications and surpasses that of most existing studies, it can be concluded that the LBM-LES numerical method demonstrates acceptable accuracy for weakly compressible airflow and can be considered a viable numerical approach for the following unsteady simulations of eVTOL aircraft. Currently, the validation is limited to thrust and torque of a single isolated rotor at various rotational speeds, limited by accessible experimental and measurement techniques.

C. Geometric model and computational setup

1. eVTOL design and configuration

A compound-wing configuration of the eVTOL aircraft is designed with reference to various commercial eVTOL models. The model measures 4.975 m in length (L) and 1.603 m in height (H). The fixed-wing uses a rectangular wing with a NACA 2412 aerofoil, a chord length of 1.2 m and a wingspan (W) of 8 m, resulting in a reference wing area of 9.6 m^2. There are no aerodynamic control surfaces (e.g. ailerons, flaps, rudder or elevator) on the simplified eVTOL model, because this study focuses on the inherent stability of the aircraft, and all the control surfaces should be in the neutral position. Each wing has a pylon mounted beneath its mid-span, each equipped with two coaxial counter-rotating lift rotors at the front and rear. A rear-mounted propeller group with two coaxial counter-rotating propellers is installed at the aft end of the fuselage. Both tail propellers have a three-blade configuration with a diameter of 1.72 m and a twist angle of 12°. For simplicity, the material is considered to be of uniform density, thereby the geometric centre is regarded as

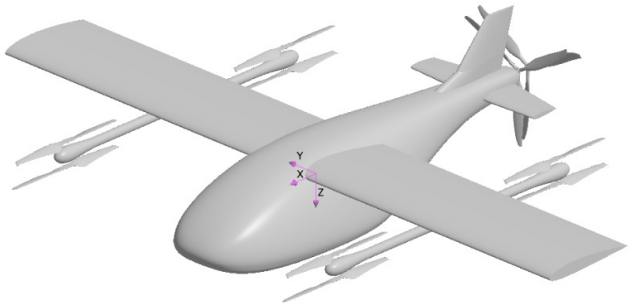

FIG. 5. The eVTOL CAD model with its local coordinate system.

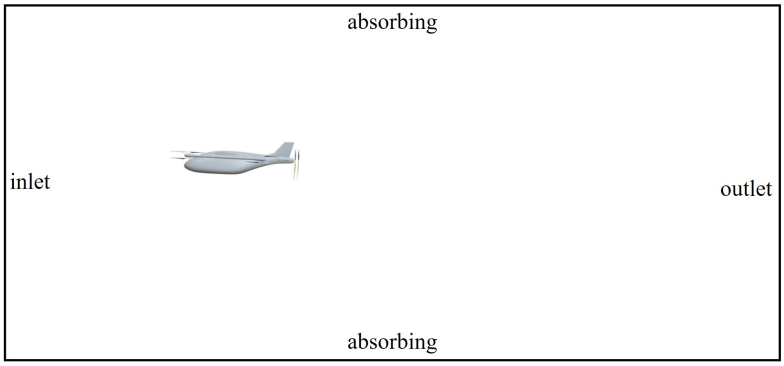

FIG. 6. Computational domain and boundary conditions of the eVTOL aircraft simulation.

the centre of gravity (CoG) of the aircraft. Thus, the origin of both the body axis system and the air-path axis system is located at the geometric centre. The geometric model and its body axis system are shown in Fig. 5, with the coordinate origin at CoG. In the following sections, $W/2$ is adopted as the characteristic length for non-dimensionalisation, with the superscript asterisks denoting dimensionless quantities.

2. *Computational domain and boundary conditions*

The computational domain measures 35 m in length, 20 m in width and 16 m in height, yielding a cross-sectional area of 320 m^2. The blockage ratio is 0.7875%, calculated by $A_{\mathrm{eVTOL,x}}/A_{\mathrm{section,x}}$, which is regarded as sufficiently small. On the surface of the aircraft, the near-wall model proposed by Liu et al.[43] is applied within the bounce-back scheme as the boundary condition. The node-refilling method[45] is employed to update new fluid nodes generated within the computational domain due to the rotation of the tail propellers. The boundaries of the rectangular fluid domain except the inlet and outlet are treated with an absorbing boundary condition, which allows fluid to exit freely without reflecting pressure waves. A free-stream velocity of 60 m/s is imposed at the inlet boundary, which is regarded as reference velocity for non-dimensionalisation. Therefore, the Reynolds number based on the wing chord and cruise speed is $Re_c = 4.6 \times 10^6$. The tail propeller speed is set to 2000 rpm, in which case the tip Mach number can be estimated as $Ma_{\mathrm{tip}} = 0.55$ using the rotational speed, propeller disk diameter, free-stream velocity and acoustic velocity, and it is in the weakly-compressible regime (i.e. $0.3 < Ma_{\mathrm{tip}} < 0.7$). The advance ratio is $J = 1.05$. The simulation condition parameters are summarized in Tab. I. The computational domain and boundary conditions are shown in Fig. 6.

The physical continuum is ideal gas with a reference density of 1.18415 kg/m, a reference pressure of 1.01325×10^5 Pa and a reference temperature of 300 K. The WALE SGS model[44] is em-

ployed in the simulation. A test case with an AoA of 3° and an angle of sideslip of 0° is adopted. The forces acting on the fuselage are observed to have stabilised under these conditions. Therefore, a physical time of 0.5 s satisfies the convergence requirement and is used for all the following simulations.

For studies on longitudinal stability, simulations are typically conducted at a fixed angle of sideslip while varying AoA to investigate the variation of pitch moment coefficient with AoA[6,8]. For studies on lateral and directional stability, AoA is set to the cruise condition, and simulations are performed at various angles of sideslip to analyse the changes in yaw moment coefficient and roll moment coefficient with respect to the angle of sideslip[6,8,10]. The simulation conditions of AoA and angle of sideslip selected for different static stability analyses in this study are listed in Table II. To simplify the expression and improve readability, AoA and angle of sideslip are denoted by the symbols α and β, respectively.

3. LBM mesh strategy

Since the collision and streaming processes in LBM rely on local interactions among discrete lattice nodes and their immediate neighbours, and the regular structure of Cartesian grids, which facilitates the streaming step of the distribution functions, naturally aligns with the discrete velocity directions of the LBM, a structured Cartesian grid strategy is employed. However, due to limited computational resources, achieving close conformity with curved solid boundaries through extreme grid refinement is often impractical. Therefore, the immersed boundary method[46] is adopted. This method discretises both the fluid domain and the solid interior with computational nodes. By comparing the positions of these nodes with the closed solid boundary, each node is classified as belonging to either the fluid domain or the solid structure.

The details of grid setup for the LBM-based eVTOL simulation in this study are configured as follows. The minimum grid resolution is 3 mm, with a total of 7 multi-resolution levels, similar to which of the single rotor simulation. Four layers of overlap grids are incorporated to facilitate numerical transition. A wake refinement zone is configured behind and below the fuselage of aircraft, extending 1 m in both directions, which is specifically targeted at the near-wake region where the most significant turbulence and interactions occur. The total count of grid cells is approximately 167 million. A mesh convergence study is conducted to eliminate the influence of cell counts on the simulation results, performed on a single NVIDIA A800 80GB GPU. By adjusting the minimum lattice size, five distinct sets of grids with varying refinement levels are generated. The mesh quality is assessed by the convergence of the lift coefficient C_L and drag coefficient C_D, given by

$$\begin{aligned} C_L &= \frac{L}{\frac{1}{2}\rho U_\infty^2 A_x}, \\ C_D &= \frac{D}{\frac{1}{2}\rho U_\infty^2 A_x}, \end{aligned} \tag{10}$$

where F_x and F_z are the total drag and lift force, respectively. Additionally, ρ is the density of the air, U_∞ is the free stream velocity, and A_x is the projected area in the free stream direction. The convergence rate is defined by

$$\mathrm{Cov}_{C_i} = \frac{C_i^{\text{current}}}{C_i^{\text{finest}}}, \tag{11}$$

Non-dimensional parameter	Value
Cruise speed (m/s)	60
Reynolds number Re_c	4.6×10^6
Tip Mach number Ma_{tip}	0.55
Advance ratio J	1.05

TABLE I. Governing parameters of conditions.

Static stability	AoA (°)	angle of sideslip (°)
Longitudinal stability	-9, -6, -3, 0, 3, 6, 9	0
Directional stability	3	-9, -6, -3, 0, 3, 6, 9
Lateral stability	3	-9, -6, -3, 0, 3, 6, 9

TABLE II. Overview of simulation conditions for static stability analysis.

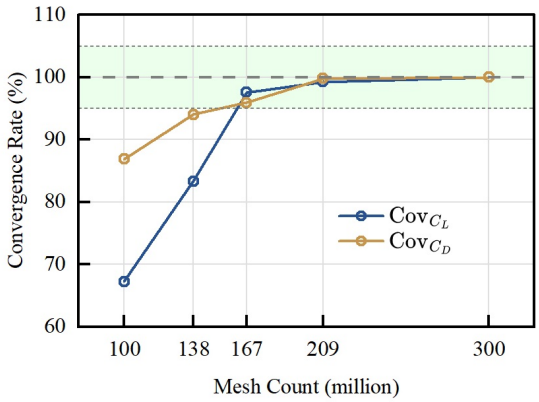

FIG. 7. Mesh convergence study for eVTOL simulations.

and is shown in Fig. 7. It can be seen that C_D and C_L remain unchanged with further reduction in the minimum lattice size once it reaches 3.0 mm. Considering the balance between simulation accuracy and computational efficiency, this size is selected for all subsequent eVTOL simulations in this study.

To further validate the mesh strategy towards a satisfactory LES configuration, two approaches are applied. First, the mesh resolution is also evaluated using two-point correlation in a series of continuously-distributed probes behind the tip of propeller, referring to Davidson[47]. The normalized two-point correlation is given by

$$C_{U_i}^{\text{norm}}(\vec{x}_0,\vec{x}) = \frac{\overline{U_i'(\vec{x}_0)\,U_i'(\vec{x})}}{U_{i\text{RMS}}'(\vec{x}_0)\,U_{i\text{RMS}}'(\vec{x})},\ U_{i\text{RMS}}'(\vec{x}_i) = \overline{U_i'(\vec{x}_i)^2}^{1/2}, \tag{12}$$

where $\vec{x}_o$ and $\vec{x}$ are the spatial coordinates of the reference point and the current point, respectively, and U_i is the local velocity in the i^{th} direction. In our study, the reference point is located at (-7.05,0,-0.86) m, following with other 19 continuous points spacing in single mesh size (Figure 8(a)). It is recommended that the largest eddies should be resolved by at least eight cells, corresponding to a positive correlation for a minimum of 8 cells. The correlation versus stride number of cells is presented in Figure 8(b). It is shown that, the correlation with the reference point remains high for the first 15 cells, demonstrating a reasonable resolution of the mesh in our study. Furthermore, the spectral kinetic energy density at the wavenumber vector $\mathbf{k}$ is defined as

$$e(\mathbf{k}) = \frac{1}{2}\left(|\widehat{u}(\mathbf{k})|^2 + |\widehat{v}(\mathbf{k})|^2 + |\widehat{w}(\mathbf{k})|^2\right), \tag{13}$$

where $\widehat{\mathbf{u}}(\mathbf{k}) = \mathscr{F}\{\mathbf{u}'(\mathbf{x})\}$ denotes the Fourier transform of the velocity-fluctuation field $\mathbf{u}'$, with $\mathbf{u}' = \mathbf{u} - \langle\mathbf{u}\rangle$. The corresponding three-dimensional isotropic (one-dimensional) energy spectrum is obtained by averaging over all wavevectors with identical magnitude $k = \|\mathbf{k}\|$, such that the total kinetic energy satisfies $\int_0^\infty E(k)\,\mathrm{d}k = \int_{\mathbb{R}^3} e(\mathbf{k})\,\mathrm{d}\mathbf{k}$, equivalently,

$$E(k) = \int_{\|\mathbf{k}\|=k} e(\mathbf{k})\,\mathrm{d}S_{\mathbf{k}} = k^2 \int_{4\pi} e(k,\Omega)\,\mathrm{d}\Omega, \tag{14}$$

as shown in Figure 8(c). To assess consistency with the Kolmogorov $-5/3$ inertial-range scaling, we additionally compute the compensated spectrum $k^{5/3}E(k)$. The Nyquist wavenumber k_N and the

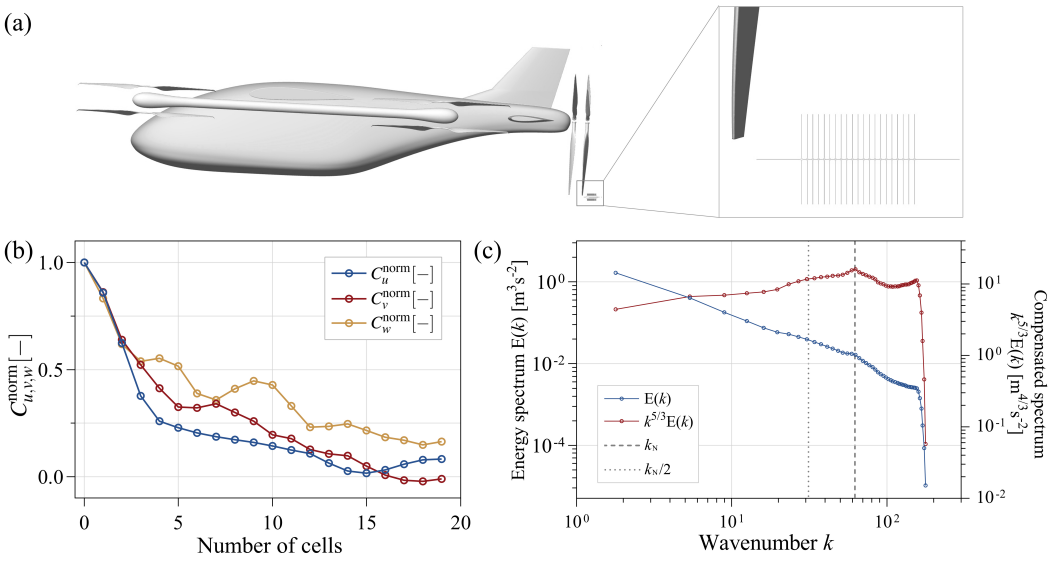

FIG. 8. Turbulence statistics verification. (a) Reference and computed points for correlation convergence study, (b) Convergence of two-point correlation $C^{\text{norm}}_{u,v,w}$ versus stride number of cells, and (c) energy spectrum $E(k)$ and compensated spectrum $k^{5/3}E(k)$.

reference limit $k_N/2$ are marked. From the figure, the energy spectrum remains strictly positive and varies smoothly over the entire set of resolved wavenumber range, with no spurious oscillations and discontinuities. For wavenumbers below $k_N/2$, $E(k)$ exhibits an approximately power-law decay and the compensated spectrum forms a broad, near-horizontal plateau, consistent with Kolmogorov inertial-range -5/3 scaling. This behavior indicates that the LES resolves a physically meaningful inertial cascade over a substantial portion of the spectrum. At high wavenumber end, there is no anomalous upturn, demonstrating no spectral pile-up (spectral blocking) or aliasing-driven energy accumulation. Overall, the spectral shape supports that the resolved range is physically consistent and that no grid-scale instabilities are present.

III. RESULTS

In this section, the dominant flow structures of this eVTOL aircraft are first analysed, followed by an evaluation of its static stability in longitudinal, directional and lateral directions.

A. Flow structures

The presentation of results on flow fields starts from the Euler vortices indicated by dimensionless Q-criterion (Fig. 9) during its cruise flight at $\alpha = 3^\circ$ and $\beta = 0^\circ$, in this context, the lift rotors stay inactive, aligning with the streamwise direction. Because the variations in AoA and sideslip angle are relatively small, the fundamental characteristics of the vortex system structure remain largely unchanged, with only minor differences in details and relative proportions. Therefore, only the flow structures under this condition are analysed in detail. Considering the need to balance the post-processing computational cost of hundred-million-cell grids with vortex identification performance, we employ the Q-criterion to capture three-dimensional vortical structures, which is defined using the velocity gradient tensor:

$$\nabla \mathbf{u} = \mathbf{S} + \mathbf{\Omega}, \quad \text{where} \quad \mathbf{S} = \frac{1}{2}\left(\nabla \mathbf{u} + (\nabla \mathbf{u})^T\right) \quad \text{and} \quad \mathbf{\Omega} = \frac{1}{2}\left(\nabla \mathbf{u} - (\nabla \mathbf{u})^T\right). \tag{15}$$

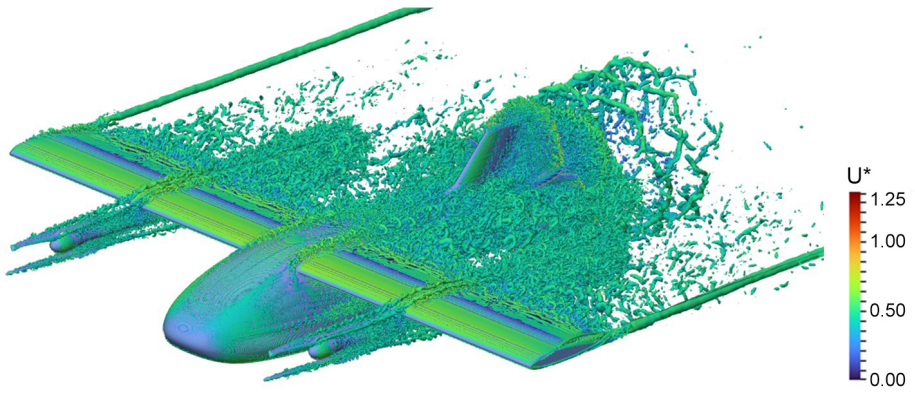

FIG. 9. Q-criterion isosurface ($Q^* = 10^4$ and 10^5) of eVTOL aircraft under $\alpha = 3^\circ$ and $\beta = 0^\circ$, coloured by velocity magnitude.

Here, $\mathbf{S}$ is the symmetric strain-rate tensor and $\mathbf{\Omega}$ is the asymmetric rotation-rate (spin) tensor. The Q-criterion is then the second invariant of $\nabla\mathbf{u}$, often written as:

$$Q = \frac{1}{2}\left(\|\mathbf{\Omega}\|^2 - \|\mathbf{S}\|^2\right). \tag{16}$$

A region in which $Q^* > 0$ is often identified as a vortex, on the premise that local rotation $\|\mathbf{\Omega}\|$ dominates over strain $\|\mathbf{S}\|$. Four kinds of vortical structures dominate the surrounding and wake flow of the aircraft. Multiple Q-criterion thresholds are tested, and the flow structures are shown to be insensitive to the values. Accordingly, $Q^* = 10^4$ and 10^5 are used to facilitate clear visualization.

First, the eight lift rotors are aligned parallel to the directional axis of the aircraft, each producing a pair of counter-rotating vortices at their edges. Among these, the tip vortices generated by the two upper-front rotors are influenced by the fixed-wing and advect along its upper surface, whereas those originating from the two lower-front rotors remain farther from the wing due to the package alignment of the eVTOL aircraft. In addition, a pair of counter-rotating vortices develops at the wing-fuselage junction, which gradually merges downstream with smaller vortices shed from the rear fuselage.

Another distinct vortical structure forms at the wingtips, exhibiting high core vorticity and thus a broader region of influence, with larger Q-criterion isosurface diameters than other stable vortex structures. Fig. 10 shows a single dominant wingtip vortex that rolls up immediately aft of the tip and remains attached to the trailing edge in the near field. The constant thickness tip and the absence of winglets allow strong lateral pressure relief, thereby the crossflow wraps around the tip early and close to the surface. The vortex is fed by three visible streams that converge at the trailing edge. One stream curls from the forward segment of the tip onto the suction side. A second stream issues from the region aft of maximum thickness along the suction side where the boundary layer is locally thick and is swept outward to the tip. A third stream originates on the pressure side, turns around the tip, and enters the roll up, supplying most of the circulation. The blunt, constant thickness tip yields relatively thick initial shear layers, therefore the nascent vortex exhibits a larger core radius and rapid early radial growth. In addition, intermittent small fragments convected with the main tip vortex, arising where the tip shear layers meet and peel into the spiral sheet. Therefore, the wingtip vortex lasts for a long distance with high stability. Finally, the tail propellers generate two intertwined double-helical vortices at the blade tips, which are known as the tip vortex of propellers. Due to the aft-mounted propulsion configuration, the stability of the thrust propeller's tip vortices is relatively poor, evidently influenced by the upstream vortex structures. Examination of the isosurfaces based on the Q-criterion reveals that the vortex tubes are discontinuous and dissipate almost completely within merely three to four vortex helix pitches.

The velocity magnitude on the symmetry plane and the C_p on both the symmetry plane and the fuselage surface are shown in Fig. 11a-b, respectively. The oncoming stream decelerates against the rounded nose and terminates in a distinct stagnation region, visible as the near-zero velocity spot,

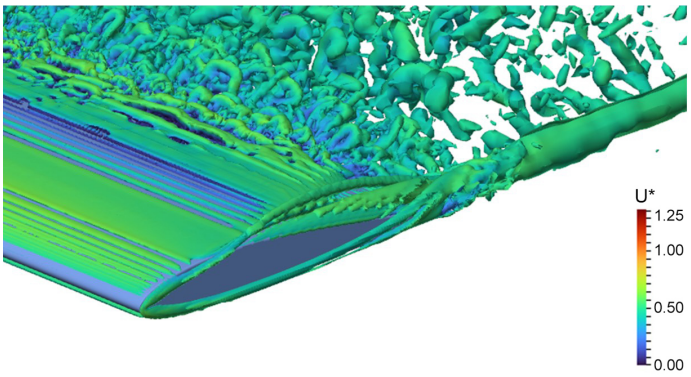

FIG. 10. Q-criterion isosurface ($Q^* = 10^4$ and 10^5) at the wingtip under $\alpha = 3^\circ$ and $\beta = 0^\circ$, coloured by velocity magnitude.

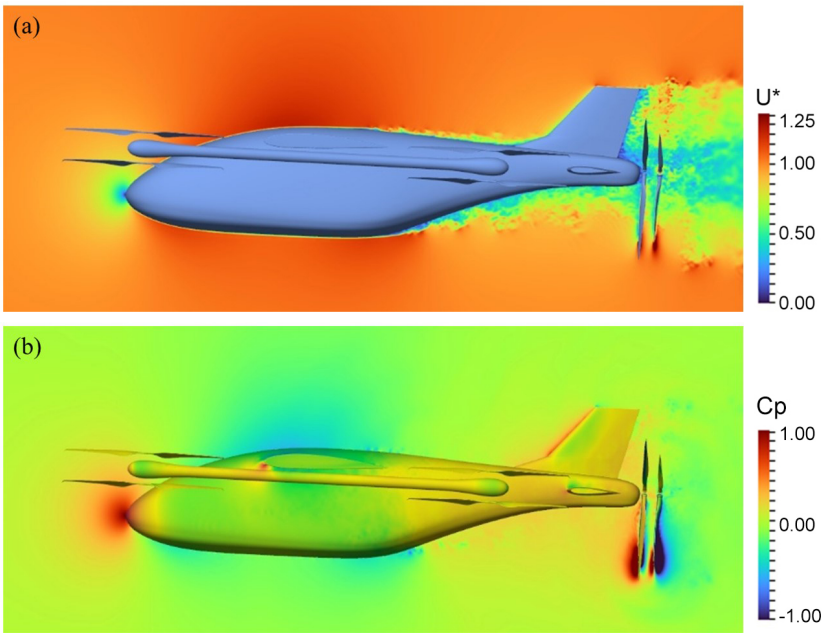

FIG. 11. Velocity and C_p of the eVTOL aircraft under $\alpha = 3^\circ$ and $\beta = 0^\circ$. (a) U^* and (b) C_p.

which sets the stagnation streamline that divides the upper and lower surface flows. Downstream of the nose the flow accelerates over the crown of the fuselage, producing a low-C_p band on the upper surface, while the lower surface maintains relatively higher C_p. This top to bottom pressure imbalance yields a modest positive normal force on the fuselage at the analysed incidence. Forebody to afterbody, the pressure recovers. The recovery on the lower afterbody imposes an adverse pressure gradient, and the velocity map shows a thickening low-speed layer with a local deficit immediately upstream of the empennage, consistent with boundary-layer separation on the lower aft fuselage and the onset of a momentum-deficit wake. The combination of high static pressure at the forebody and reduced static pressure over the afterbody identifies the fore to aft pressure differential as the dominant contributor to fuselage form drag under this condition.

Furthermore, Fig. 12 presents the Q-criterion isosurface of the eVTOL aircraft in a top view during cruising, focusing on the thrust propellers operating within the wake region of the fuselage, where its flow velocity is reduced due to the fuselage blockage. Therefore, the propeller blades experience a larger local effective AoA compared to front-mounted propulsion configuration, resulting in relatively higher blade efficiency, which is also known as the boundary layer ingestion

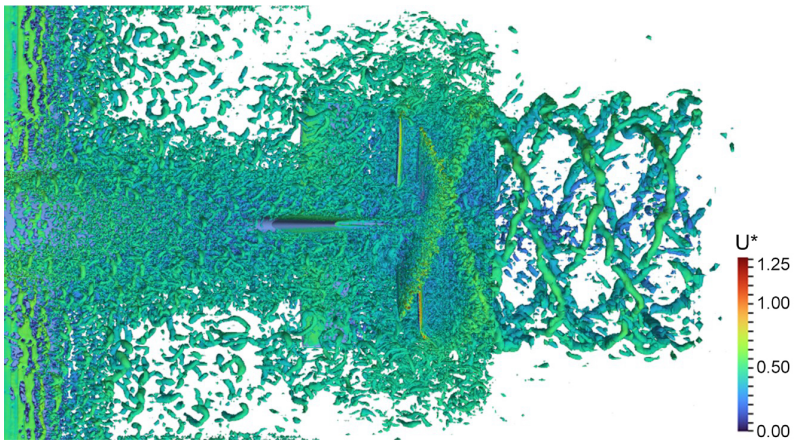

FIG. 12. Q-criterion isosurface ($Q^* = 10^4$ and $Q^* = 10^5$) of the eVTOL aircraft in a top view under $\alpha = 3^\circ$ and $\beta = 0^\circ$.

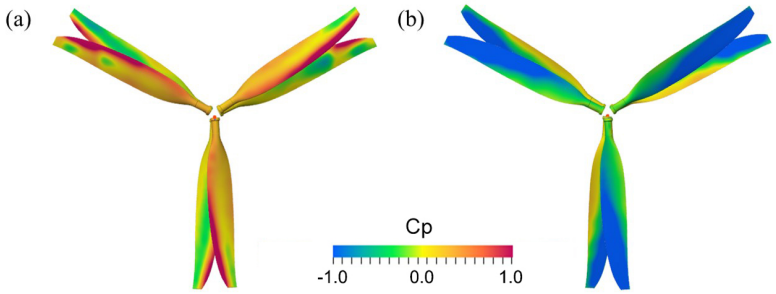

FIG. 13. Surface C_p contour of the tail propellers. (a) Pressure surface, (b) suction surface.

propulsion[48]. Furthermore, for the counter-rotating propellers, the wake formed by their tip vortices exhibits two interwoven double-helical patterns, where the two tip vortices interact with each other and demonstrate stronger instability, and thereby can only persist shortly, see Fig 9. Fig. 13 further illustrates the difference in surface C_p between the windward side and the leeward side of the tail propellers. For the reasons discussed above, the pressure on the windward side of the propellers is higher than that on the leeward side, reducing the thrust by the tail-mounted propulsion system. In addition, because the blade rotational speed is relatively low near the root, the resulting inflow velocity induces local flow separation on the leeward side of the blade, leading to partial pressure recovery in this region. This effect partly reduces the pressure drag behind, and around the propeller hub and thereby mitigates thrust depreciation.

To expose rotor-wing interference mechanisms that are muted at a low AoA, we examine a higher AoA where adverse pressure gradients promote separation and the rotor-induced vortex more clearly delays stall while altering longitudinal stability. Fig. 14 presents the velocity contours on longitudinal sections at $y^* = 0.5$ (through the lift rotors with support structures and fixed-wing) and $y^* = 0.625$ (only going through the fixed-wing) at $\alpha = 9^\circ$ and $\beta = 0^\circ$. By comparing the velocity distribution near the upper wing surface, it is evident that the vortex shed from the upper front lift rotor convects close to the upper wing surface, which delays separation on the upper surface at high AoA while simultaneously generating a stable vortex-induced lift there. Although this vortex-induced lift can postpone wing stall to some extent, it also shifts the wing’ s centre of pressure forward, which may adversely affect the aircraft’ s longitudinal stability.

With a further increase in angle of sideslip, Fig. 15 illustrates the development of rotor-tip vortices from the upper-front lift rotors at $\alpha = 3^\circ$ and $\beta = 6^\circ$, where notable flow structures emerge. Two vortical tubes form near the windward blade tip of the upper-front rotors, representing a variant

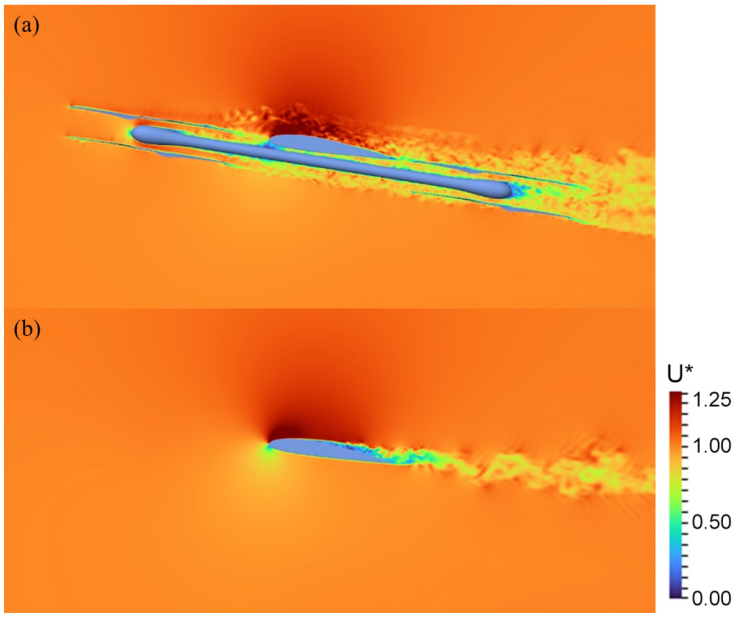

FIG. 14. Velocity contours on longitudinal sections of eVTOL under $\alpha = 9^\circ$ and $\beta = 0^\circ$. (a) $y^* = 0.5$ and (b) $y^* = 0.625$.

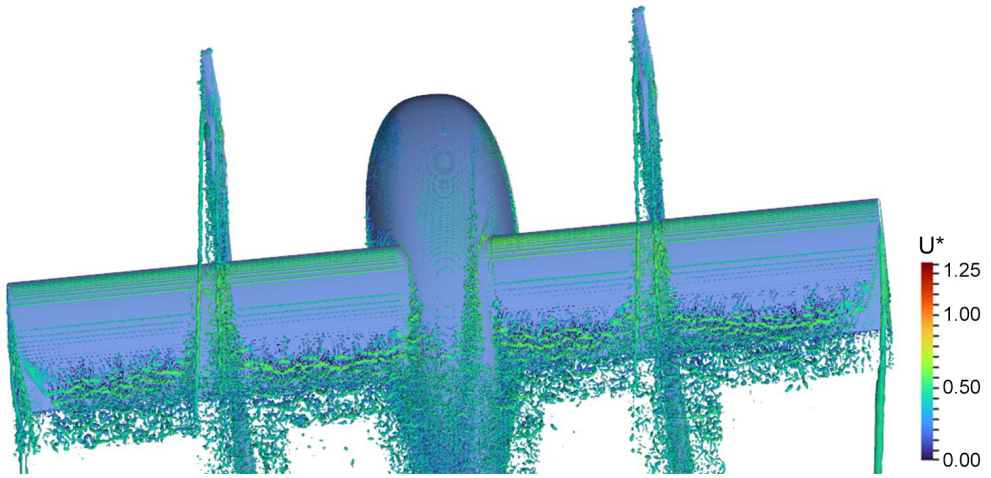

FIG. 15. Q-criterion isosurface ($Q^* = 10^4$ and $Q^* = 10^5$) from top view of eVTOL under $\alpha = 3^\circ$ and $\beta = 6^\circ$.

of the tip-vortex pair discussed above. One tube is the conventional tip vortex shed where bound circulation terminates at the blade tip and, once detached, convects with the free stream. The second tube originates on the windward edge near the tip but remains semi-attached to the rotor. Local acceleration around the windward tip and the curvature of the separating shear layer supply axial core momentum that delays complete roll-up and detachment, yielding an orientation closer to the heading direction. As both tubes convect into the fixed-wing influence region, the spanwise pressure gradient on the upper surface and the pre-existing downwash impose an outward deflection. The resulting strain aligns and thins the vortices, after which they merge with the wingtip and trailing-edge vortex system and undergo rapid breakdown through Kelvin–Helmholtz instability and viscous diffusion.

B. Static stability

1. Longitudinal stability

Longitudinal stability refers to the ability of an aircraft to return to level flight state within the symmetric plane[49]. For a longitudinally stable aircraft, an increase in the AoA induces an increase in the negative pitching moment (nose-down tendency), which will reduce the AoA in turn, expressed in Eq. 17:

$$\frac{\mathrm{d}C_m}{\mathrm{d}\alpha} < 0, \tag{17}$$

where C_m is pitching moment coefficient. The pitching moment coefficient is defined as

$$C_m = \frac{M}{\frac{1}{2}\rho v^2 S_\mathrm{W} c_\mathrm{A}}, \tag{18}$$

where M is the pitching moment, ρ is the air density, v is the incident flow velocity, S_W is the wing reference area which is the product of the span and chord length for a rectangular wing, and c_A is the mean geometric chord of the wing.

The variation of the pitching moment coefficient with AoA for this eVTOL aircraft is shown in Fig. 16. For the overall aircraft, as the AoA increases, the pitching moment coefficient also increases, resulting in a positive $C_{m_\alpha} = \partial C_m / \partial \alpha$, which is the key criterion for instability determination. At negative AoA, the curve of the overall aircraft remains below zero, which means that the aircraft generates a nose down pitching moment that has to be balanced by the flight control system or by suitable trim settings. As the AoA approaches 0°, the pitching moment coefficient of the complete configuration tends to zero, which confirms that the calculated condition corresponds to a trimmed state close to level flight. In the range from $\alpha = 0°$ to about $\alpha = 6°$, the increase of C_m with α is nearly linear, therefore this interval governs the static longitudinal behaviour in typical low speed climb and conversion flight. The curve corresponding to the fuselage and wing is very close to the curve of the overall aircraft over the entire AoA range. This confirms that the aerodynamics of these components is responsible for almost all of the destabilizing gradient. The curve associated with the propellers stays nearly horizontal and slightly above zero, which indicates that the propulsive system contributes a small nose up moment but does not vary with AoA in a significant way. This is because the thrust line is located near the CoG and the inflow variation with AoA is limited, therefore, the propellers do not provide an AoA dependent stabilizing contribution. For $\alpha > 6°$, the slope of the overall curve decreases. This behaviour can be related to the onset of local flow separation or to changes in the effective interference between lifting surfaces, which

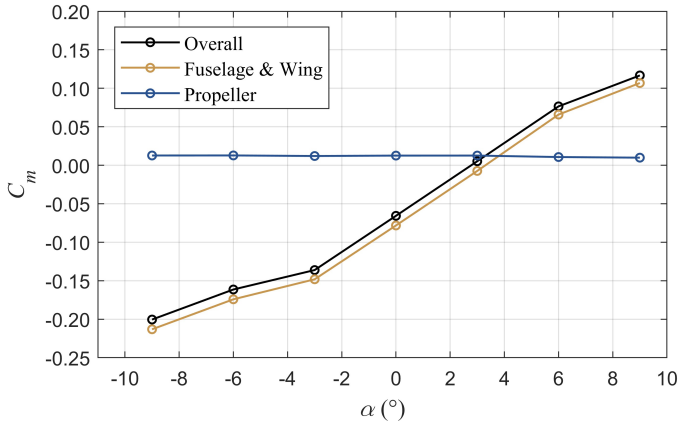

FIG. 16. Variation of pitching moment coefficient with AoA.

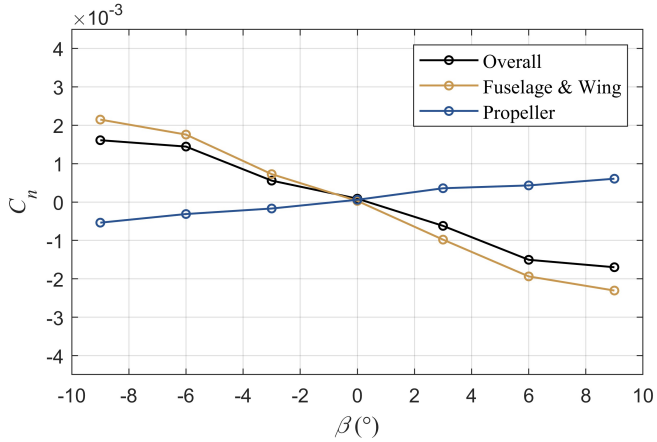

FIG. 17. Variation of yawing moment coefficient with angle of sideslip.

reduce the rate at which the nose up moment grows. The aircraft therefore remains longitudinally unstable, although the instability is moderated at higher AoA. This characteristic is favourable for operation near the maximum lift condition because it prevents an excessive nose up tendency that would require large control surface deflections or very aggressive automatic stabilization.

To enhance the longitudinal stability of the eVTOL configuration, several approaches can be adopted, such as adjusting the mass distribution of the fuselage, relocating the fixed-wing rearwards, and increasing the horizontal tail area, so as to position the CoG in front of the aerodynamic centre. Within a certain range of AoA, lift increases with AoA. This increased lift generates a nose-down moment, thereby providing the aircraft with longitudinal restoring characteristics. In addition, lowering the installation position of the tail propellers can align their thrust line with the aircraft CoG, eliminating the influence of the longitudinal force exerted on propellers on the aircraft's overall longitudinal stability. While there are several potential improvements regarding longitudinal stability worth investigating, a detailed quantitative study is not present in this study, since our focus remains on the advantages of LBM as a numerical method for eVTOL simulations rather than a specific aircraft design.

2. *Directional stability*

Directional stability refers to the tendency of an aircraft to return to its equilibrium in yaw[49]. For an aircraft that possesses directional stability, a positive increase in angle of sideslip, which means the aircraft is slipping to the right, generates a positive yawing moment that turns the nose to the right. This yawing moment acts to reduce the angle of sideslip, as expressed in Eq. 19:

$$C_{n_\beta} = \frac{\partial C_n}{\partial \beta} > 0 \tag{19}$$

where C_n is yawing moment coefficient. The yawing moment coefficient is defined as:

$$C_n = \frac{N}{\frac{1}{2}\rho v^2 S_W b} \tag{20}$$

where N is yawing moment, and b is the wing span of the eVTOL aircraft.

The variation of the yawing moment coefficient with angle of sideslip for this eVTOL aircraft is shown in Fig. 17. For the overall aircraft, as the angle of sideslip increases, the yawing moment coefficient decreases, leading to negative C_{n_β} which indicates an unstable state in directional direction. Similar to C_m, the fuselage and wing are the primary sources of the overall directional instability among all the components, while the propellers provide a slight positive contribution to directional

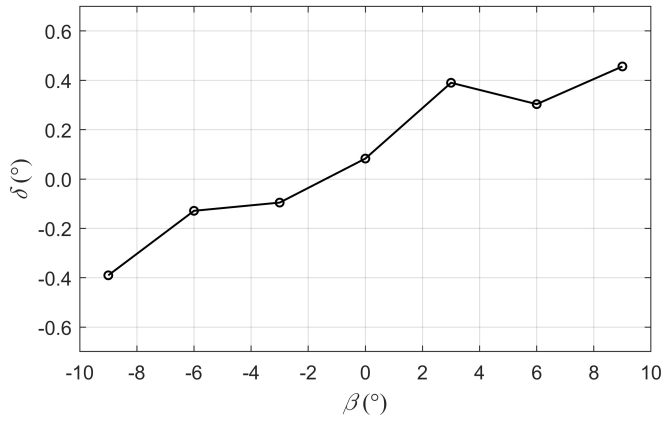

FIG. 18. Variation of the direction of the horizontal component of the tail propeller force and the aircraft angle of sideslip.

stability. However, the overall yawing moment coefficients remain relatively small by comparison with the study of Kim[8] on distributed-propulsion aircraft, thereby the eVTOL aircraft in this paper exhibits a mild degree of directional instability.

Furthermore, as shown in Fig. 18, when the angle of sideslip increases, the angle between the horizontal component of the tail propeller force and the aircraft longitudinal axis also increases, indicating that the aerodynamic force acting on the tail rotor deflects in response to the incident flow direction. Since the tail propellers are located relatively far aft of the aircraft's CoG, when the aircraft is facing lateral incident flow, the aerodynamic force on the tail propellers produces a yawing moment about the centre of gravity that turns the aircraft toward the flow, thus reducing the angle of sideslip. Therefore, the tail propellers contribute to the directional stability of the aircraft during the flight. However, the directional stability provided by the tail propellers is obviously insufficient to counteract the directional instability induced by the fuselage. Moreover, when the propellers produce sufficient thrust, they may even exhibit a directionally unstable characteristic.

Generally, the directional stability of fixed-wing aircraft is guaranteed by the restoring moment provided by the vertical tail. In this case, Fig. 9 shows that the vertical tail is enveloped by the burst shed vortices from the fixed wing and the tip vortices from the tail propeller. Consequently, the airflow in the vicinity of the vertical tail is characterised by low velocity and high turbulence, leading to a significant loss in total pressure. When the vertical tail operates within this energy-deficient flow, the lateral force generated on its surface is drastically reduced. As a result, the restoring moment of the aircraft under sideslip conditions decreases substantially, which is incapable of providing sufficient directional stability for the eVTOL aircraft.

Therefore, to enhance the directional stability of this eVTOL configuration, the vertical tail area should be increased to strengthen the yawing moment generated by the vertical tail under oblique free-stream conditions, thereby enabling the aircraft to yaw toward the incoming flow. In-depth quantitative analysis of the optimisation for directional stability of eVTOL aircraft remains to be focused in our future study.

3. Lateral stability

Lateral stability refers to the resistance to instability of an aircraft in the roll direction[49]. For an aircraft possessing lateral stability, when the angle of sideslip increases positively, a negative rolling moment is generated, which will reduce the angle of sideslip:

$$C_{l_\beta} = \frac{\partial C_l}{\partial \beta} < 0, \tag{21}$$

where C_l is rolling moment coefficient:

$$C_l = \frac{L}{\frac{1}{2}\rho v^2 S_W b}, \tag{22}$$

where L is rolling moment. The variation of the rolling moment coefficient with angle of sideslip for the eVTOL aircraft is shown in Fig. 19. For the aircraft as a whole, the rolling moment coefficient decreases as the angle of sideslip increases, indicating that the aircraft tends to roll about its CoG in a direction that reduces the angle of sideslip, thereby exhibiting lateral stability. The fuselage and wing structures constitute the primary sources of this overall lateral stability, whereas the tail propeller exhibits a slight and secondary tendency toward lateral instability.

From the perspective of the surface pressure as shown in Fig. 20, when the eVTOL aircraft operates at a non-zero angle of sideslip, the upwind (right, in this case) wing exhibits a lower surface pressure and a larger low-pressure region on its upper surface compared with the opposite wing, while the pressure difference on the lower surface is relatively small. Consequently, the pressure difference between the upper and lower surfaces of the right wing is greater than that of the left wing, generating a rolling moment about the aircraft's longitudinal axis. When the aircraft begins to roll to the right from level flight, the lift vector tilts to the right, causing the aircraft to yaw to the right and produce a positive angle of sideslip. The increased lift on the right wing then produces a negative rolling moment that induces leftward roll, thereby creating a tendency to return

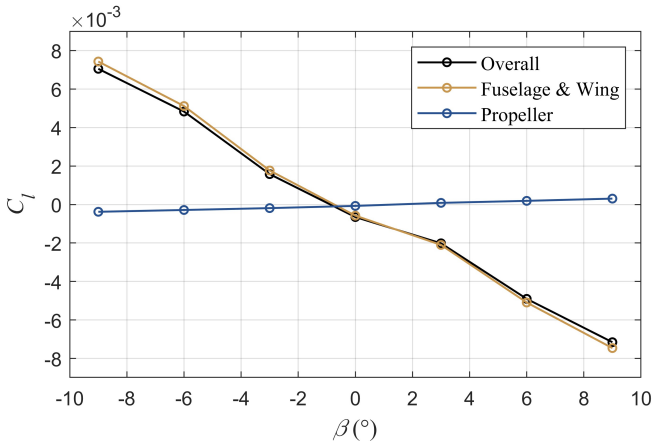

FIG. 19. Variation of rolling moment coefficient with angle of sideslip.

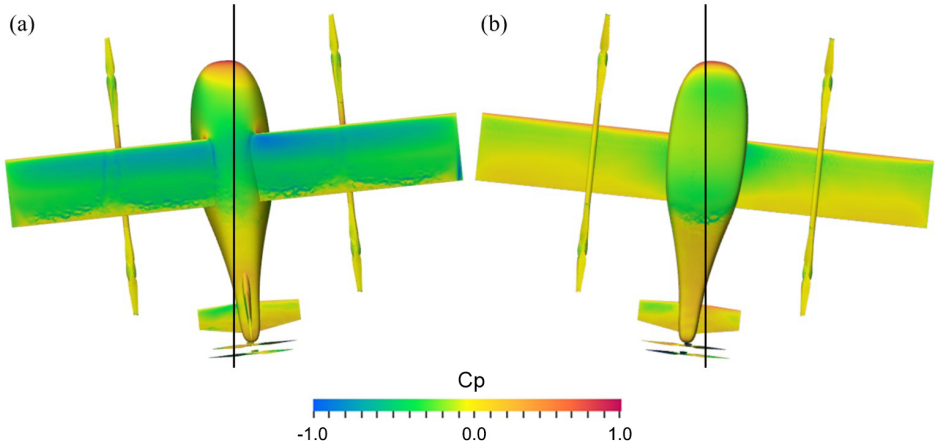

FIG. 20. Surface pressure contour of eVTOL aircraft ($\alpha = 3°$, $\beta = 6°$). (a) Top view, (b) bottom view.

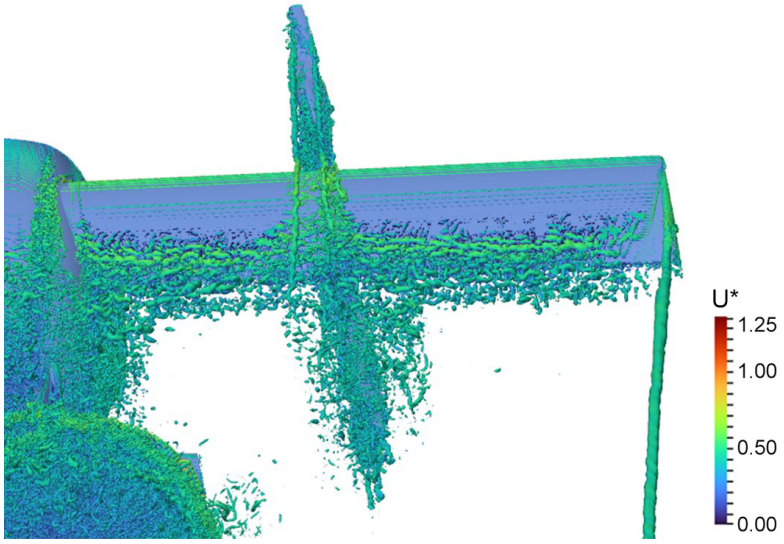

FIG. 21. Q-criterion isosurface ($Q^* = 10^4$ and $Q^* = 10^5$) above the right wing under $\alpha = 3°$, $\beta = 6°$.

to the level state.

Additionally, Fig. 21 shows that the wingtip vortex of the upwind wing rolls upward and moves toward the upper surface behind the wingtip. The low-pressure vortex core remains attached to the upper surface of the wing and generates vortex-induced lift, thereby contributing to the lateral stability of the aircraft to some extent. However, the vortex shed from the upper front lift rotor deflects laterally along the incident flow direction. The vortex is attached to the upper surface of the fixed-wing again, and the position of the low-pressure region induced by this vortex structure shifts consequently (Fig. 20a), leading to a change in the distribution of vortex-induced lift. This variation reduces the magnitude of the negative rolling moment at positive angles of sideslip, thereby exhibiting a slightly adverse influence on the lateral stability of the aircraft, although the effect is not pronounced and the global lateral stability still maintained.

Notably, while the eVTOL aircraft lacks inherent longitudinal and directional stability, such static instability is acceptable in modern aircraft design, given that control can be maintained via closed-loop feedback mechanisms, including active control surfaces, thrust vectoring and AI-driven flight control laws.

IV. CONCLUSION

While previous studies primarily focused on flight stability analysis of fixed-wing aircraft and rotorcraft based on FVM, few studies employed LBM method as a high-fidelity numerical method to analyse the flight stability of eVTOL aircraft, which have novel configurations, or the wake interactions that dominant the phenomenon. Based on LBM numerical method, this study reveals the typical vortical structures of an eVTOL aircraft, investigates the static stability, and analyses the dictating flow mechanisms, including the flow characteristics surrounding the tail propellers.

In this study, the numerical performance of FVM-LES and LBM-LES is first validated and compared by simulating an eVTOL lift rotor and comparing with test-stand experimental results. Based on the LBM-LES, further numerical simulations are conducted for a specific eVTOL configuration to analyse its flow-field structures and static stability. The main conclusions are summarised below:

(1) For weakly compressible flows surrounding an eVTOL aircraft, LBM-LES is capable of accurately capturing the influence of compressibility on aerodynamic forces with an numerical error below 11% for thrust and below 7% for torque regarding rotor simulations. The sim-

ulations based on LBM-LES are 8∼9 times faster than those based on FVM-LES for the same physical time, which exhibits significant advantages in computational efficiency and cost compared with FVM-LES.

(2) Four main categories of vortex structures dominate the flow field of eVTOL aircraft, including wingtip vortices, wing root vortices, tip vortices from lift rotors, and tail propeller tip vortices. The wingtip vortices form through convergence of three flow components at the trailing edge and positively influence lateral stability. The wing root vortices gradually merge with vortices from the rear fuselage. The tip vortices from the upper front lift rotors adhere to the upper wing surface, delaying flow separation and wing stall, yet adversely affecting both longitudinal and lateral stability. The tail propeller tip vortices form a pair of typical intersecting double-helical structures.

(3) When the tail-propeller rotational speed is insufficient, the propellers produce significantly reduced thrust, indicating that the compound-wing configuration eVTOL with tail-mounted propulsion imposes stringent performance requirements on the thrust power system.

(4) The eVTOL demonstrates lateral stability. This is because the wing encountering the incoming flow earlier has a lower surface pressure and a larger low-pressure region on its upper surface compared with the opposite wing. Furthermore, the tip vortex on this side rolls upward toward the upper surface, generating additional vortex-induced lift. Consequently, the lift on the earlier flow-encountering wing becomes greater, inducing a restoring rolling moment that promotes a tendency to reduce sideslip and roll.

(5) The eVTOL aircraft examined in this study exhibits longitudinal instability during cruise. In directional, the aircraft is mildly unstable. That is mainly because the vertical tail, enveloped by low-energy, highly-turbulent flow induced by the fixed-wing and tail-propeller vortices, produces much lower lateral force and restoring moment under sideslip. Nevertheless, the drag acting on the propellers tends to align them with the oncoming flow, imparting a weathervane effect that partially augments directional stability. This indicates that compared with conventional low-speed aircraft, the typical aerodynamic configurations of eVTOL aircraft pose greater challenges to the control system, which must be compensated through appropriate control law design with advanced fly-by-wire systems. In addition, since static stability is closely related to the safety margin of the eVTOL aircraft, we encourage relevant industry personnel to refine the standards before full commercialisation of eVTOL aircraft so as to take this factor into account.

(6) For eVTOL aircraft development, LBM-LES is highly recommended for high-fidelity unsteady simulations where complex moving boundaries, such as rotors, and rapid turnaround time are prioritised. Nevertheless, it should be noted that LBM-LES encounters inherent limitations when simulating supersonic flow regimes, where FVM-LES may still offer superior robustness and advantages.

(7) In light of the identified longitudinal and directional static instabilities, we recommend incorporating advanced strategies such as active control, thrust vectoring, and AI-driven control laws into the eVTOL design. Enhancing controllability in this manner is crucial for eVTOL aircraft, given their role as small-scale civil aircraft operating in low-altitude airspace.

Based on our existing findings, our subsequent research will further focus on the scaled wind tunnel testing of the eVTOL aircraft to validate the simulation results further, as well as on the dynamic stability derivatives calculated via simulations of oscillatory motions such as phugoid and plunging modes. Meanwhile, we are aim at developing a workflow for the rapid iterative development of eVTOL aircraft using LBM-based CFD simulations.

DISCLOSURE STATEMENT

No potential conflict of interest was reported by the authors.

FUNDING

This work was supported by Shanghai Key Laboratory of Aerodynamics and Thermal Environment Simulation for Ground Vehicles under Grant No. 23DZ2229029.

ACKNOWLEDGMENTS

The authors acknowledge AEROCAE Digital Technology, Ltd. for their support on LBM-based CFD software, GPU resources for partial simulations in this study, and fruitful discussions as well. The authors acknowledge T-Motor team for their technical support.

AUTHORSHIP CONTRIBUTION STATEMENT

R.Mo: Formal analysis, Investigation, Methodology, Software, Validation, Writing - original draft, Data curation, Writing - review & editing, Visualization. Q.Zhou: Software, Data curation, Visualization. Q.Jia: Conceptualization, Methodology, Supervision, Funding acquisition, Project administration. C.Xia: Supervision, Writing - review. H.Wei: Conceptualization, Supervision, Investigation, Validation, Writing - review. Z.Yang: Supervision, Resources. All authors reviewed and approved the final version of the manuscript to be published and agree to be accountable for all aspects of the work.

DATA AVAILABILITY STATEMENT

Data supporting the findings of this study are available from the corresponding author upon reasonable request.

REFERENCES

[1]N. Polaczyk, E. Trombino, P. Wei, and M. Mitici, "A review of current technology and research in urban on-demand air mobility applications," in *8th Biennial Autonomous VTOL technical meeting and 6th Annual electric VTOL Symposium*, Vol. 28 (Vertical Flight Soc. Mesa, Arizona, 2019) pp. 333–343.

[2]L. He, S. Yang, W. Zhang, Y. Zhao, and L. Wang, "Research on fuselage aerodynamic configuration wind tunnel test of hybrid highspeed helicopter with single main rotor," Aeronautical Science and Technology **34**, 62–69 (2023).

[3]Y. Wang, *Research on Flight Characteristics of Intermeshing Rotor Helicopter*, Master's thesis, Nanjing University of Aeronautics and Astronautics (2021).

[4]L. Luan, *Stability and Control Analysis of Compound Helicopter Powered by Twin Propellers*, Master's thesis, Nanjing University of Aeronautics and Astronautics (2021).

[5]Z. Wang, P. Li, B. Wang, Z. Zhu, and C. Liu, "Variation of tilt-rotor aircraft motion stability and its influence mechanism," Journal of Aerospace Power , 1–15 (2024).

[6]A. Jirásek, R. M. Cummings, A. Schütte, and K. Huber, "Extended assessment of stability and control prediction methods for nato air vehicles: Summary," Journal of Aircraft **55**, 623–637 (2018).

[7]E. Seaver, C. J. Bennett, and N. Lawson, "Flight testing of the effects of airspeed and aircraft configuration in lateral-directional static stability for a jetstream 31," in *AIAA AVIATION 2023 Forum* (American Institute of Aeronautics and Astronautics, 2023).

[8]D. Kim, Y. Lee, S. Oh, Y. Park, J. Choi, and D. Park, "Aerodynamic analysis and static stability analysis of manned/unmanned distributed propulsion aircrafts using actuator methods," Journal of Wind Engineering and Industrial Aerodynamics **214**, 104648 (2021).

[9]S. J. Kim, Y.-H. Hwang, R. S. Myong, and H. Lee, "Interactional aerodynamics and acoustics of a rotor with an airframe in hover," Physics of Fluids **36**, 017121 (2024).

[10]N. van Arnhem, R. de Vries, T. Sinnige, R. Vos, and L. L. M. Veldhuis, "Aerodynamic performance and static stability characteristics of aircraft with tail-mounted propellers," Journal of Aircraft **59**, 415–432 (2022).

[11]J. Thiemeier, C. Öhrle, F. Frey, M. KeSSler, and E. Krämer, "Aerodynamics and flight mechanics analysis of airbus helicopters' compound helicopter racer in hover under crosswind conditions," CEAS Aeronautical Journal **11**, 49–66 (2020).

[12]X. Gao, S. Jing, W. Wang, T. Yang, X. Chen, and Q. Zhao, "Numerical investigation of the aeroacoustic mechanisms of loading noise induced by dynamic stall of rotor airfoils," Physics of Fluids **37**, 097137 (2025).
[13]N. Roh, S. Oh, and D. Park, "Aerodynamic characteristics of helicopter with ducted fan tail rotor in hover under low-speed crosswind," International Journal of Aerospace Engineering **2020**, 7059209 (2020).
[14]X. Wang, S. Li, and C. Lin, "Aerodynamic characteristics of helicopter with leadingedge slatted horizontal tail," Journal of Nanjing University of Aeronautics and Astronautics **52**, 288–293 (2020).
[15]H. Sun, P. Sun, Y. Yang, M. Yuan, F. Fan, and Y. Lin, "Analysis of aerodynamic characteristics of helicopter biplane tailplane," Journal of Northwestern Polytechnical University **42**, 232–240 (2024).
[16]H. Qi, W. Du, T. Pu, N. Zheng, and W. Zhu, "Aerodynamic interactions between coaxial rotor and obstacle in hover," Physics of Fluids **37**, 096137 (2025).
[17]D. Su, G. Xu, S. Huang, and Y. Shi, "Numerical investigation of rotor loads of a shipborne coaxial-rotor helicopter during a vertical landing based on moving overset mesh method," Engineering Applications of Computational Fluid Mechanics **13**, 309–326 (2019).
[18]R. B. Green, E. A. Gillies, and R. E. Brown, "The flow field around a rotor in axial descent," Journal of Fluid Mechanics **534**, 237–261 (2005).
[19]S. Chae, S. Lee, and J. Kim, "Effects of rotor–rotor interaction on the wake characteristics of twin rotors in axial descent," Journal of Fluid Mechanics **952**, A31 (2022).
[20]Y.-B. Lee and J.-S. Park, "Hover performance analyses of coaxial co-rotating rotors for evtol aircraft," Aerospace **9** (2022), 10.3390/aerospace9030152.
[21]T. C. A. Stokkermans, D. Usai, T. Sinnige, and L. L. M. Veldhuis, "Aerodynamic interaction effects between propellers in typical evtol vehicle configurations," Journal of Aircraft **58**, 815–833 (2021).
[22]B. M. Simmons and P. C. Murphy, "Aero-propulsive modeling for tilt-wing, distributed propulsion aircraft using wind tunnel data," Journal of Aircraft **59**, 1162–1178 (2022).
[23]A. Zanotti and D. Algarotti, "Aerodynamic interaction between tandem overlapping propellers in evtol airplane mode flight condition," Aerospace Science and Technology **124**, 107518 (2022).
[24]Z. Gao, S. Zheng, S. Zhang, H. Wang, X. Shao, and L. Zeng, "Aerodynamic characteristics study on multiple propellers in distributed electric propulsion configurations," Physics of Fluids **37**, 015131 (2025).
[25]M. S. Araghizadeh, B. Sengupta, S. M. Son, H. Lee, and R. S. Myong, "Atmospheric turbulence inflow effect on the aerodynamics and aeroacoustics of side-by-side urban air mobility aircraft," Physics of Fluids **37**, 107105 (2025).
[26]S. M. Son, C.-H. Song, M. S. Araghizadeh, R. S. Myong, and H. Lee, "Investigation of aerodynamics, wake dynamics, and aeroacoustic characteristics of a full-configuration tiltrotor aircraft during transition flight," Physics of Fluids **37**, 107133 (2025).
[27]J. Liu, G. Li, D. Ma, and F. Wang, "Aerodynamic interference and wake characteristics of a multirotor tandem tilt-wing electric vertical take-off and landing aircraft in conversion flight," Physics of Fluids **37**, 115127 (2025).
[28]J. Deng, Y. Yang, W. Liao, J. Zhu, X. Wang, and C. Xu, "An aerodynamic characterization of tilt-rotor aircraft wings based on wind tunnel tests," Physics of Fluids **37**, 087101 (2025).
[29]C. Luan and Y. Lei, "Aerodynamic study of dihedral angle configurations on a hexacopter during horizontal airflow disturbances," Physics of Fluids **37**, 105108 (2025).
[30]G. Bucherelli, L. Das, D. Granata, and A. Zanotti, "Mid-fidelity numerical investigation of the interactional aerodynamic mechanisms in an electrical vertical take-off and landing quad-rotor aircraft," Physics of Fluids **37**, 067138 (2025).
[31]L. Sun, X. Liu, Q. Tao, and J. Yang, "Aerodynamic performance of ducted fans for large-scale electric propulsion aircraft under variable operating conditions," Physics of Fluids **37**, 035184 (2025).
[32]M. Chang, Z. Zheng, X. Meng, J. Bai, and B. Wang, "Aerodynamic analysis of a low-speed tandem-channel wing for evtol aircraft considering propeller–wing interaction," Energies **15** (2022), 10.3390/en15228616.
[33]J. Kim, S. Lee, and D. Im, "Conceptual design of two-seater lift & cruise type urban air mobility," in *AIAA SCITECH 2024 Forum* (American Institute of Aeronautics and Astronautics, 2024).
[34]W. Xian and A. Takayuki, "Multi-gpu performance of incompressible flow computation by lattice boltzmann method on gpu cluster," Parallel Computing **37**, 521–535 (2011).
[35]L. Boltzmann, "Weitere studien über das wärmegleichgewicht unter gasmolekülen," in *Kinetische Theorie II: Irreversible Prozesse Einführung und Originaltexte* (Vieweg+Teubner Verlag, Wiesbaden, 1970) pp. 115–225.
[36]S. Chen, Z. Wang, X. Shan, and G. D. Doolen, "Lattice boltzmann computational fluid dynamics in three dimensions," Journal of Statistical Physics **68**, 379–400 (1992).
[37]P. L. Bhatnagar, E. P. Gross, and M. Krook, "A model for collision processes in gases. i. small amplitude processes in charged and neutral one-component systems," Phys. Rev. **94**, 511–525 (1954).
[38]S. G. Ashok, S. Hosseini, and J. Rauleder, "Real-time dynamic inflow model for a coaxial helicopter configuration using the lattice–boltzmann method," in *AIAA SCITECH 2024 Forum* (American Institute of Aeronautics and Astronautics, 2024).
[39]M. Chávez-Modena, J. L. Martínez, J. A. Cabello, and E. Ferrer, "Simulations of aerodynamic separated flows using the lattice boltzmann solver xflow," Energies **13** (2020), 10.3390/en13195146.
[40]S. Hou, Q. Zou, S. Chen, G. Doolen, and A. C. Cogley, "Simulation of cavity flow by the lattice boltzmann method," Journal of Computational Physics **118**, 329–347 (1995).
[41]C. Lyu, W. Li, M. Desbrun, and X. Liu, "Fast and versatile fluid-solid coupling for turbulent flow simulation," ACM Trans. Graph. **40** (2021), 10.1145/3478513.3480493.
[42]C. Lyu, K. Bai, Y. Wu, M. Desbrun, C. Zheng, and X. Liu, "Building a virtual weakly-compressible wind tunnel testing facility," ACM Trans. Graph. **42** (2023), 10.1145/3592394.
[43]M. Liu, K. Bai, and X. Liu, "A hybrid near-wall model for kinetic simulation of turbulent boundary layer flows," ACM Trans. Graph. **44** (2025), 10.1145/3730829.

[44]F. Nicoud and F. Ducros, "Subgrid-scale stress modelling based on the square of the velocity gradient tensor," Flow, Turbulence and Combustion **62**, 183–200 (1999).
[45]A. Caiazzo, "Analysis of lattice boltzmann nodes initialisation in moving boundary problems," Progress in Computational Fluid Dynamics An International Journal **8**, 3–10 (2008).
[46]C. S. Peskin, "Flow patterns around heart valves: A numerical method," Journal of Computational Physics **10**, 252–271 (1972).
[47]L. Davidson, "Large eddy simulations: How to evaluate resolution," International Journal of Heat and Fluid Flow **30**, 1016–1025 (2009), the 3rd International Conference on Heat Transfer and Fluid Flow in Microscale.
[48]D. Hall, A. Huang, A. Uranga, E. Greitzer, M. Drela, and S. Sato, "Boundary layer ingestion propulsion benefit for transport aircraft," Journal of Propulsion and Power **33**, 1–12 (2017).
[49]R. H. Barnard and D. R. Philpott, *Aircraft flight: A description of the physical principles of aircraft flight*, 4th ed. (Prentice Hall, Harlow, England, 2010).